J Mater Sci (2008) 43:7445–7450
DOI 10.1007/s10853-008-2774-z

ULTRAFINE-GRAINED MATERIALS

Microstructural investigation of AA 2195 T81 chips formed during a metal-cutting process

Lei Dong · Judy Schneider

Received: 21 February 2008 / Accepted: 2 June 2008 / Published online: 21 July 2008

Abstract In this study, the microstructure of AA 2195 T81 metal-cutting chips formed during a turning operation were characterized using microscopy and diffraction techniques. At a constant strain of 2, the resulting strain rate imposed on the metal was varied from 0.8×10^4 to 2.6×10^5 s^{-1}. At strain rate of 0.8×10^4 s^{-1}, the resulting microstructure contained regions of 100 nm ultrafine grains. At the highest strain rate of 2.6×10^5 s^{-1}, 150–200 nm ultrafine grains were observed plus overaged precipitates. The grain size increment and appearance of overaged precipitates with the higher strain rate is conjectured to be a result of temperature increment and not of direct strain rate.

Introduction

High strength-to-weight ratio properties combined with corrosion resistance make aluminum alloys one of the most commonly used metals in the automotive and aerospace industries [1]. Of particular interest to the aerospace community is AA2195, an Al–Cu–Li alloy which offers a decrease in density with an increase in stiffness. Additional strength improvements can be realized in these alloys if the microstructure can be refined from micron to ultrafine or nano-grains. To realize this improved strength, various thermo-mechanical methods have been investigated for the production of ultrafine and nano-grained materials. One thermo-mechanical process commonly used is equal-channel angular pressing (ECAP) [2–7], where grain refinement has been achieved in several commercial aluminum alloys including: 1100, 2024, 3004, 5084, 6061, and 7075 [8–11]. In these studies, refinement of the grain size to less than 1 μm was achieved over a range of effective strains from 2 to 10. In these studies the effective strain rate was not reported, only the pressing speed for the metal deformation in the range of $\sim$19 mm s^{-1} [8]. Although uniform grain sizes are achieved in the ECAP process, the requirement for multiple passes is time intensive.

Ultrafine grains have also been reported in the microstructure of metal-cutting chips [12–18]. This technique has been suggested as an alternative process for producing nano-grained materials which can be consolidated to retain the nano-structure [19]. In a research by Shankar et al. [15], 100–200 nm grains were reported in the metal-cutting chips of an AA 6061 alloy. The machining parameters imparted a range of strain from 3 to 5 over a range of strain rates from 10^2 to 10^3 s^{-1}.

This study further explores the critical processing parameters that result in effective grain refinement. While grain refinement was observed over the range of strain rates investigated, a corresponding change in precipitation kinetics also affected the final microstructure.

Experimental procedure

This study utilizes metal cutting to impose a strain rate from 0.8×10^4 to 2.6×10^5 s^{-1}, at a constant strain of 2, to an AA2195 T81 alloy. Figure 1 illustrates the orientation of the specimen discs machined from a rolled plate of 12.7-mm thick AA 2195 T81. The nominal alloying chemistry of this aluminum alloy in wt.% is: 4.19 Cu, 0.95 Li, 0.29 Mg,

L. Dong (✉) · J. Schneider
Department of Mechanical Engineering, Mississippi State University, Mississippi State, MS 39762, USA
e-mail: ld225@msstate.edu; lei.dongleiekin@gmail.com

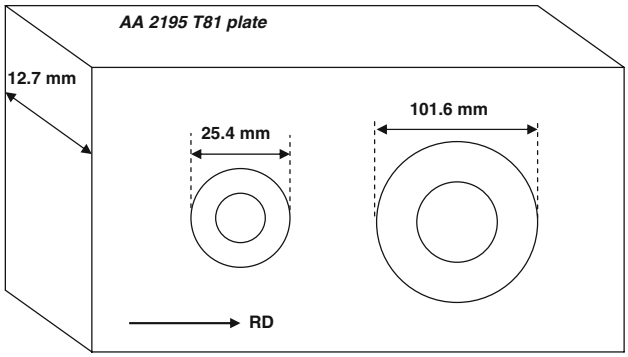

Fig. 1 Machining specimen orientation with respect to PM-rolled plate

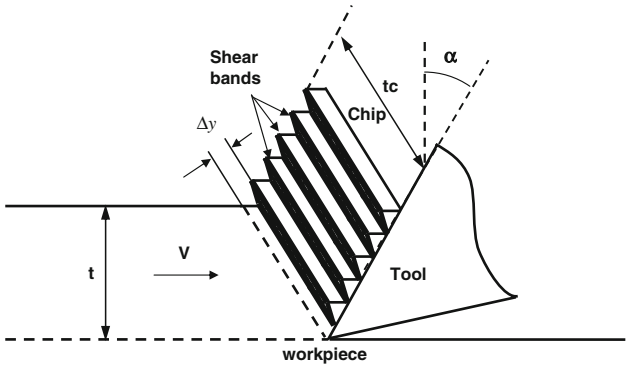

Fig. 3 Classic orthogonal metal cutting schematic

0.31 Ag, and 0.12 Zr. A center hole in the machining specimen ensured a free surface at both ends of the cutting tool. The initial parent material (PM) contained pancake-shaped grains approximately 1–2 mm long by 250–500 μm wide. Previous orientation image mapping (OIM) results revealed a predominant $\{110\}\langle 112\rangle$ rolling texture for the PM [20] with complimentary TEM studies confirming the presence of T_1 (Al_2CuLi) and θ' (Al_2Cu) precipitates [21].

The specimen disks were mounted on a lathe, as shown in Fig. 2, with the cutting tool perpendicular to the longitudinal axis of the specimen disc. Orthogonal cutting tests were performed at cutting speeds of 0.20, 2.66, and 5.32 m/s which correspond to strain rates of 0.8×10^4, 1.6×10^5, and 2.6×10^5 s^{-1}, respectively. The depth of cut and a 2° rake angle were kept constant during the turning operation. As the metal chips were cut, an alcohol quench was applied to retain the microstructure. A schematic of the orthogonal cutting process is illustrated in Fig. 3. By measuring the cutting speed (V), depth of cut (t), chip thickness (t_c), and shear band spacing (Δy), the strain (γ) and strain rate ($\dot{\gamma}$) can be calculated using Eqs. 1 and 2, respectively [22],

$$\gamma = \frac{\cos\alpha}{\sin\phi \cdot \cos(\phi - \alpha)} \tag{1}$$

$$\dot{\gamma} = \frac{\cos\alpha}{\cos(\phi - \alpha)} \cdot \frac{V}{\Delta y} \tag{2}$$

where the shear angle (ϕ), a geometric relationship, is calculated using Eq. 3 [22]:

$$\tan\phi = \frac{\frac{t}{t_c}\cos\alpha}{1 - \frac{t}{t_c}\sin\alpha} \tag{3}$$

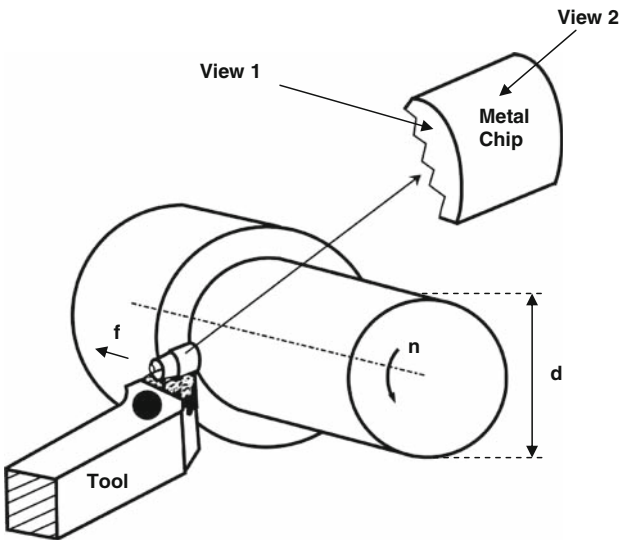

Fig. 2 Schematic of chip formation during the turning process

Figure 2 illustrates the side and cutting surface of the metal-cutting chip, labeled view 1 and 2, respectively. Representative metal-cutting chips from both views were metallurgically mounted and polished to investigate the microstructure. A Keller's regent etch was used to reveal the microstructure for optical microscopy (OM) and scanning electron microscopy (SEM). The OM images were recorded using a LEICA DMI 5000 metallographic light microscope with differential interference contrast (DIC). SEM images were obtained by using a JOEL 6500F field emission (FE)-SEM operating at 5 kV. An energy dispersive spectrometer (EDS), mounted on the FE-SEM, was used for elemental analysis.

Because of the metal-cutting chip size, transmission electron microscopy (TEM) specimens were only cut from view 2. TEM specimen disks (3 mm) were punched from the thinned foil, dimpled on both sides, and ion-milled to electron transparency. The TEM specimens were examined in a JEOL JEM-100CX TEM operated at an accelerating voltage of 100 kV with bright-field image (BFI) and electron diffraction patterns recorded. It was assumed that any native oxides formed during the metal-cutting process were removed during specimen preparation.

A Rigaku Ultima III X-ray diffractometer (XRD) with Cu-Kα X-ray was used to investigate the texture and presence of stable precipitates in the metal-cutting chips. A

continuous scan was made at a rate of 0.035°/min over a 2θ range of 18–55°.

Results

Table 1 summarizes the turning conditions and measured metal-cutting chip parameters which were input to Eqs. 1–3 for calculating the resulting strain and strain rates. Figure 4a presents a typical OM image of view 1 of an etched AA 2195 T81 metal-cutting chip showing typical deformation flow lines observed at all cutting conditions. The metal-cutting chips show a discontinuous pattern, regularly separated by inhomogeneous shear bands, whose spacing is summarized in Table 1. Figure 4b presents a typical SEM image of view 1 of the etched AA 2195 T81 metal-cutting chip which also shows the typical flow lines. In the metal-cutting chips formed at conditions associated with the higher strain rates of 10^5 s^{-1}, light particles were observed in the SEM images and identified as copper rich using EDS. These Cu-rich particles ranged from 1 to 10 μm in size. Figure 5 shows the corresponding OM and SEM images of view 2.

Table 1 Summary of the cutting parameters and resulting shear strain and shear strain rates

Specimen diameter (d) (mm)	Depth of cut (t) (mm)	Cutting speed (m/s)	Shear band spacing (Δy) (μm)	Strain (γ)	Strain rate ($\dot{\gamma}$) (s^{-1})
25.4	0.102	0.20	40.0 ± 6.5	2.0	0.8×10^4
101.6	0.152	2.66	26.3 ± 3.5	2.0	1.6×10^5
101.6	0.152	5.32	25.5 ± 4.0	2.0	2.6×10^5

Figure 6 exhibits TEM BFIs and corresponding electron diffraction patterns (inset) of the microstructure for view 2 of representative metal-cutting chips from each condition. At a strain of 2 and a strain rate of 0.8×10^4 s^{-1}, the TEM BFI and inset electron diffraction pattern in Fig. 6b display evidence of refined grains with an average size of 100 ± 35 nm. As the strain rate is increased to 10^5 s^{-1}, the TEM BFIs in Fig. 6b and c shows a slight increase in grain

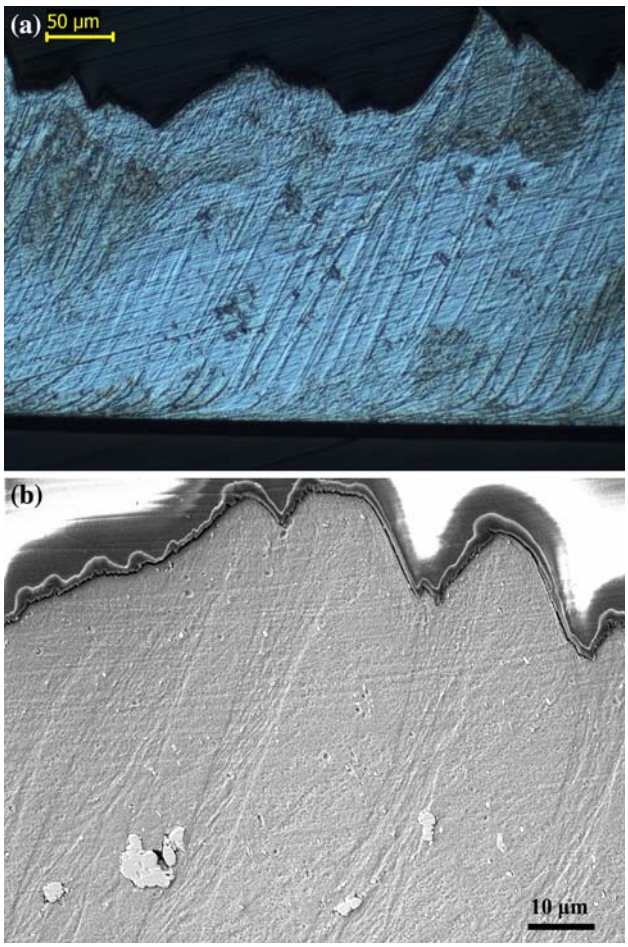

Fig. 4 Side (view 1) of the metal-cutting chip formed at 2.6×10^5 s^{-1}: (**a**) OM image and (**b**) SEM image

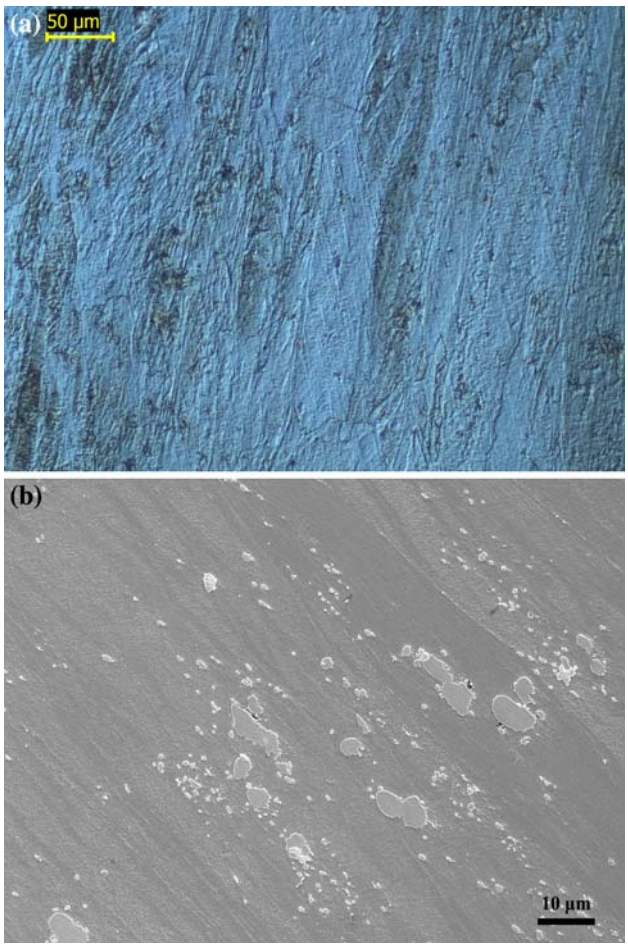

Fig. 5 Cutting surface (view 2) of the metal-cutting chip formed at 2.6×10^5 s^{-1}: (**a**) OM image and (**b**) SEM image

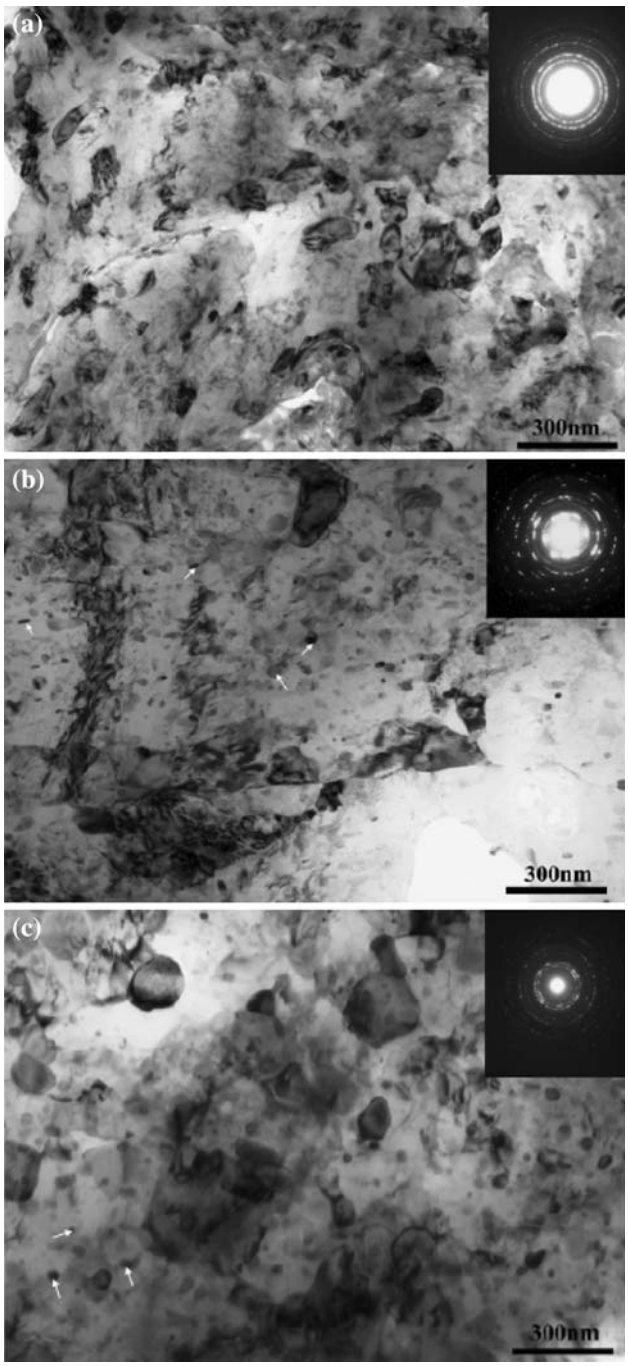

Fig. 6 TEM BFI and inset electron diffraction patterns of view 2 of the metal-cutting chips formed at: (**a**) 0.8×10^4 s^{-1}; (**b**) 1.6×10^5 s^{-1}; and (**c**) 2.6×10^5 s^{-1}. The arrows denote overaged precipitates in (**b**) and (**c**)

size to the range of 150–200 nm (180 ± 70 and 160 ± 55 nm, respectively). However, in addition to the ultrafine grains, the TEM BFI for these specimens also shows the presence of overaged precipitates, both round and rod shaped.

The phase content of the PM and the metal-cutting chips was also examined by XRD. The XRD results are shown in Fig. 7. T_1 and θ' phases were present in the Al matrix of the PM. After imposition of a strain rate of 0.8×10^4 s^{-1}, these phases can no longer be detected in the Al matrix. At the higher strain rates of 1.6×10^5 and 2.8×10^5 s^{-1}, Al_2Cu (θ), Al_7Cu_4Li (T_B), Al_2CuLi (T_1), and AlLi phases were detected. Reported stable phases in the AA2195 system include Al_2Cu (θ), Al_7Cu_4Li (T_B), and Al_2CuLi (T_1) [23]. The reported morphology of these stable phases [23] is consistent with the TEM BFIs in Fig. 6b and c which shows round- and rod-shaped precipitates in the metal-cutting chips.

Table 2 summarizes the change in the peak intensity ratio and the full width at half maximum (FWHM) for the Al matrix observed in the XRD patterns as a function of strain rate. The PM displays an increased intensity for the (200) reflection indicative of the texture. In all metal-cutting chips, the intensity ratios are different from both the random reference Al powder and the PM. The changes in the intensity ratio suggest that the plastic deformation induced by the metal cutting is contributing to the evolution of the crystallographic texture [25].

Discussion

Reported studies of grain refinement in ECAP relied on imposing a strain to the material in the range of 2–10 at undocumented strain rates [8–11]. In reports describing metal cutting, strains in the range of 3–5 were imposed on the metal at strain rates of 10^2–10^3 s^{-1}, with resulting grain sizes in the range of 100–200 nm. The current study was undertaken to further explore the effect of strain rate on grain refinement. Higher strain rates were imposed on the metal by metal cutting at a constant strain of 2. Prior to metal cutting, the as-received microstructure of the PM was coarse, consisting of pancake-shaped grains 1–2 mm long by 250–500 μm wide. Following the deformation induced by the metal-cutting process, grain refinement was observed in TEM BFIs ranging from 100 to 200 nm.

As the strain rate increases, so does the amount of deformational heating raising the temperature of the metal-cutting chips. With increased stored dislocation energy due to the deformation, increased temperatures benefit recovery by providing the driving energy for grain refinement while subsequently decreasing the dislocation density. The formation of slightly larger grain sizes in the metal-cutting chips formed at a strain rate range of 10^5 s^{-1} is attributed to the higher temperature achieved at high cutting speeds, causing the slight additional grain growth. Campbell et al. [26] concluded that a dynamic equilibrium structure via dislocation generation and annihilation could not occur at high strain rate conditions. Thus, new grains form via dynamic recrystallization mechanism at high strain rate

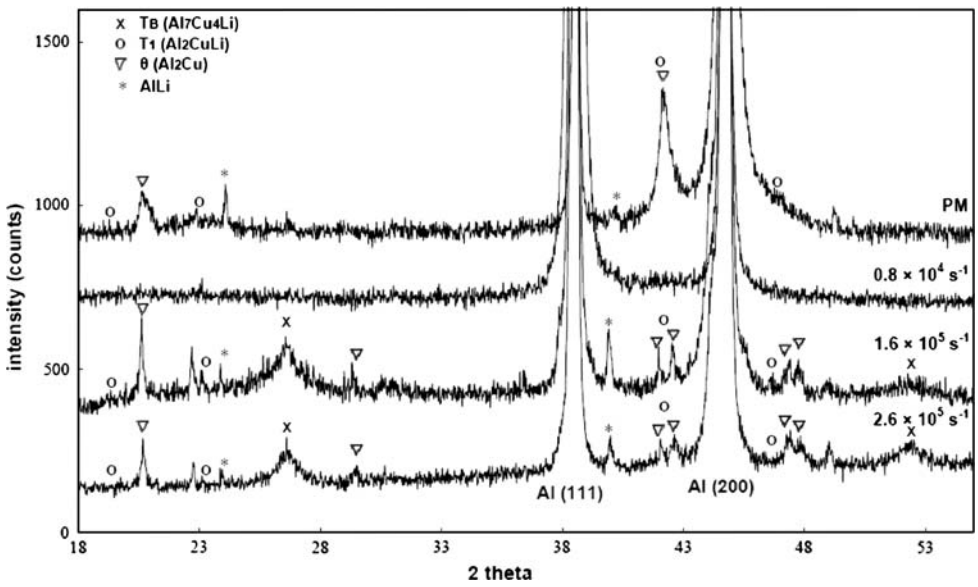

Fig. 7 XRD analysis of PM and the metal-cutting chips

Table 2 Texture variations between parent material and resulting microstructures

	{111} 2θ°	{111} FWHM	{200} 2θ°	{200} FWHM	Intensity ratio {111}/{200}
ICDD for Al [24]	38.472	–	44.738	–	2.128
PM	38.559	0.343	44.780	0.345	0.063
0.8×10^4 s^{-1}	38.520	0.410	44.799	0.466	5.376
1.6×10^5 s^{-1}	38.460	0.271	44.700	0.350	0.990
2.6×10^5 s^{-1}	38.480	0.253	44.720	0.317	0.781

conditions [26]. The strain in the metal-cutting chips is concentrated along the primary shear planes [27, 28] resulting in strain gradients. High strain energies are typically stored in these shear planes, driven by the large orientation gradients which are reported to be potential sites for recrystallization [29–32].

No peak broadening was observed in XRD results for the Al matrix summarized in Table 2, which would only be expected for microstructures containing grains less than 100 nm. The phase identification results of the XRD analysis correlate with the TEM observations in Fig. 6b and c of overaged precipitates present in the metal-cutting chips formed at 10^5 s^{-1}. As shown in Fig. 7, the corresponding T_1, θ' and AlLi metastable phases cannot be resolved in the XRD analysis of the metal-cutting chips formed at 0.8×10^4 s^{-1}. Presumably solutionization has occurred. In the metal-cutting chips formed at the higher strain rate range of 10^5 s^{-1}, the range of precipitates reported in the AA2195 system are observed [23]. In precipitation-strengthened alloys, temperature increases drive the dissolution of metastable θ', T_1, and AlLi phases. In the temperature range of 138–260 °C, re-precipitate can occur and if held for sufficient times, the stable T_B and θ phases form at the expense of T_1 and θ' [33]. At temperatures above 427 °C, the overaged, stable T_B phase forms directly [20, 33]. Thus, grains containing the T_B phase are indicative of exposure to higher temperatures occurring at the higher strain rate. As shown in Table 2, the strain rate increased in an order of magnitude from 0.8×10^4 to 2.6×10^5 s^{-1}. At the higher strain rate condition, there is insufficient time for solutionization of the precipitates. At the localized elevated temperature condition, T_1 and θ' phases can directly transform to the stable T_B phase and θ phase. Thus, the initial precipitates in the PM could not undergo the conventional solution and re-precipitation process at the shear strain rate of 10^5 s^{-1}.

Summary

Ultrafine grains in the range of 100–200 nm were formed in the metal-cutting chips of AA 2195 T81 at a strain of 2 over a range of strain rates from 0.8×10^4 to 2.6×10^5 s^{-1}. This range of grain sizes is consistent with machining studies in other Al alloys at lower strain rates [12–18]. Overaged precipitates were observed in the TEM BFIs and XRD analysis of the specimen cut at the lower strain rates near 10^5 s^{-1}, but not in the TEM BFIs and XRD analysis of the specimen cut at the lower strain rates near 10^4 s^{-1}. The precipitates observed at higher strain

rates are attributed to higher temperatures. Presence of the stable T_B phase among the higher strain rate precipitates suggests temperatures above 427 °C. This indicates that insufficient time exists for the conventional solution and re-precipitation process at strain rates of 10^5 s^{-1}.

This implies that if processing parameters are selected for grain refinement, limiting the strain rate to $<10^5$ s^{-1} avoids the presence of overaged precipitates in the final microstructure.

Acknowledgements The authors wish to thank Mr. Curtis Bahr at the NASA-MSFC for fabrication of the test specimens. The authors wish to acknowledge the funding provided by the 2007 NASA Summer Faculty Program #NNM05AA22A and the AFOSR Grant FA9550-07-1-0282.

References

1. Kaufman JG (2000) Introduction to aluminum alloys and tempers. ASM International, Materials Park
2. Valiev RZ, Islamgaliev RK, Alexandrov IV (2000) Prog Mater Sci 45:103. doi:10.1016/S0079-6425(99)00007-9
3. Matsubara K, Miyahara Y, Horita Z, Langdon TG (2003) Acta Mater 51:3073. doi:10.1016/S1359-6454(03)00118-6
4. Mishra RS, Valiev RZ, McFadden SX, Mukherjee AK (1998) Mater Sci Eng A 252:174. doi:10.1016/S0921-5093(98)00684-4
5. Furukawa M, Ma Y, Horita Z, Nemoto M, Valiev RZ, Langdon TG (1998) Mater Sci Eng A 241:122. doi:10.1016/S0921-5093(97)00481-4
6. Iwahashi Y, Horita Z, Nemoto M, Langdon TG (1997) Acta Mater 45:4733. doi:10.1016/S1359-6454(97)00100-6
7. Valiev RZ, Alexandrov IV, Zhu YT, Lowe TC (2002) J Mater Res 17:5. doi:10.1557/JMR.2002.0002
8. Horita Z, Fujinami T, Nemoto M, Langdon TG (2000) Metall Mater Trans A 31:691. doi:10.1007/s11661-000-0011-8
9. Kim JK, Kim HK, Park JW, Kim WJ (2005) Scr Mater 53:1207. doi:10.1016/j.scriptamat.2005.06.014
10. Zhao YH, Liao XZ, Jin Z, Valiev RZ, Zhu YT (2004) Acta Mater 52:4589. doi:10.1016/j.actamat.2004.06.017
11. Zhao YH, Liao XZ, Zhu YT (2005) J Mater Res 20:288. doi:10.1557/JMR.2005.0057
12. Brown TL, Swaminathan S, Chandrasekar S, Compton WD, King AH, Trumble KP (2002) J Mater Res 17:2484. doi:10.1557/JMR.2002.0362
13. Swaminathan S, Shankar MR, Lee S, Hwang J, King AH, Kezar RF, Rao BC, Brown TL, Chandrasekar S, Compton WD, Trumble KP (2005) Mater Sci Eng A 410–411:358
14. Shankar MR, Chandrasekar S, King AH, Compton WD (2005) Acta Mater 53:4781. doi:10.1016/j.actamat.2005.07.006
15. Shankar MR, Chandrasekar S, Compton WD, King AH (2005) Mater Sci Eng A 410–411:364. doi:10.1016/j.msea.2005.08.137
16. Swaminathan S, Brown TL, Chandrasekar S, McNelley TR, Compton WD (2007) Scr Mater 56:1047. doi:10.1016/j.scriptamat.2007.02.034
17. Ni H, Elmadagli M, Alpas AT (2004) Mater Sci Eng A 385:267
18. Ni H, Alpas AT (2003) Mater Sci Eng A 361:338. doi:10.1016/S0921-5093(03)00530-6
19. Shigematsu I, Suzuki K, Imai T, Kwon YJ, Saito N (2005) J Mater Sci 40:2971. doi:10.1007/s10853-005-2390-0
20. Schneider JA, Nunes AC Jr (2004) Metall Mater Trans B 35:777. doi:10.1007/s11663-004-0018-4
21. Schneider JA, Nunes AC Jr, Chen PS, Steele G (2005) J Mater Sci 40:1. doi:10.1007/s10853-005-2808-8
22. Shaw MC (1984) Metal cutting principles. Oxford University Press, Clarendon
23. Schneider K, Heimendahl M (1973) Z Metallkd 64:342
24. International Centre for Diffraction Date (ICDD) PDF22006#00-004-0787
25. Puerta Velásquez JD, Bolle B, Chevrier P, Geandier G, Tidu A (2007) Mater Sci Eng A 452–453:469. doi:10.1016/j.msea.2006.10.090
26. Campbell CE, Bendersky LA, Boettinger WJ, Ivester R (2006) Mater Sci Eng A 430:15. doi:10.1016/j.msea.2006.04.122
27. Elmadagli M, Alpas AT (2003) Mater Sci Eng A 355:249. doi:10.1016/S0921-5093(03)00072-8
28. Zhang H, Alpas AT (2002) Mater Sci Eng A 332:249. doi:10.1016/S0921-5093(01)01752-X
29. Gourdet S, Montheillet F (2000) Mater Sci Eng A 283:274. doi:10.1016/S0921-5093(00)00733-4
30. Duckham A, Engler O, Knutsen RD (2002) Acta Mater 50:815. doi:10.1016/S1359-6454(02)00112-X
31. Engler O (2001) Scr Mater 44:229. doi:10.1016/S1359-6462(00)00597-2
32. Humphreys FJ (2004) Mater Sci Forum 467–470:107
33. Chen PS, Bhat BN (2002) NASA/TM 2002-211548